



HAL
open science

Range imaging observations of PMSE using the EISCAT VHF radar: Phase calibration and first results

J. R. Fernandez, R. D. Palmer, P. B. Chilson, I. Häggström, M. T. Rietveld

► To cite this version:

J. R. Fernandez, R. D. Palmer, P. B. Chilson, I. Häggström, M. T. Rietveld. Range imaging observations of PMSE using the EISCAT VHF radar: Phase calibration and first results. *Annales Geophysicae*, 2005, 23 (1), pp.207-220. hal-00317512

HAL Id: hal-00317512

<https://hal.science/hal-00317512>

Submitted on 18 Jun 2008

HAL is a multi-disciplinary open access archive for the deposit and dissemination of scientific research documents, whether they are published or not. The documents may come from teaching and research institutions in France or abroad, or from public or private research centers.

L'archive ouverte pluridisciplinaire **HAL**, est destinée au dépôt et à la diffusion de documents scientifiques de niveau recherche, publiés ou non, émanant des établissements d'enseignement et de recherche français ou étrangers, des laboratoires publics ou privés.

Range imaging observations of PMSE using the EISCAT VHF radar: Phase calibration and first results

J. R. Fernandez¹, R. D. Palmer^{1,5}, P. B. Chilson², I. Häggström³, and M. T. Rietveld⁴

¹Department of Electrical Engineering, University of Nebraska, Lincoln, NE 68588-0511, USA

²CIRES–University of Colorado and NOAA Environmental Technology Laboratory, Boulder, CO 80305-3328, USA

³EISCAT Scientific Association, Box 164, S-98123 Kiruna, Sweden

⁴Max–Planck–Institut für Aeronomie, 37191 Katlenburg–Lindau, Germany

⁵Now with the School of Meteorology, University of Oklahoma, Norman, OK 73019, USA

Received: 1 October 2003 – Revised: 16 March 2004 – Accepted: 14 April 2004 – Published: 31 January 2005

Part of Special Issue “Eleventh International EISCAT Workshop”

Abstract. A novel phase calibration technique for use with the multiple-frequency Range IMaging (RIM) technique is introduced based on genetic algorithms. The method is used on data collected with the European Incoherent SCATter (EISCAT) VHF radar during a 2002 experiment with the goal of characterizing the vertical structure of Polar Mesosphere Summer Echoes (PMSE) over northern Norway. For typical Doppler measurements, the initial phases of the transmitter and receiver are not required to be the same. The EISCAT receiver systems exploit this fact, allowing a multi-static configuration. However, the RIM method relies on the small phase differences between closely spaced frequencies. As a result, the high-resolution images produced by the RIM method can be significantly degraded if not properly calibrated. Using an enhanced numerical radar simulator, in which data from multiple sampling volumes are simultaneously generated, the proposed calibration method is validated. Subsequently, the method is applied to preliminary data from the EISCAT radar, providing first results of RIM images of PMSE. Data using conventional analysis techniques, and confirmed by RIM, reveal an often-observed double-layer structure with higher stability in the lower layer. Moreover, vertical velocity oscillations exhibit a clear correlation with the apparent motion of the layers shown in the echo power plots.

Key words. Ionosphere (polar ionosphere); Meteorology and atmosphere dynamics (middle atmosphere dynamics); Radio science (interferometry)

1 Introduction

Polar Mesosphere Summer Echoes (PMSE) are unusually strong radar echoes received from the mesosphere primarily at high latitudes. Ecklund and Balsley (1981) reported the first PMSE echoes from the mesopause region above Alaska during the mid-summer months using a mesosphere-stratosphere-troposphere (MST) Doppler VHF radar. The strength of these echoes captured the attention of the scientific community given that VHF radar signals are weakly backscattered from meter-scale irregularities of the refractive index which, in the mesosphere, are caused by fluctuations of electron density. Subsequently, PMSE echoes have been observed by several MST radars operating over a wide range of wavelengths (Hoppe et al., 1990; Bremer et al., 1996). However, these observations cannot be explained by turbulent Bragg scatter since the range of scales of observed PMSE fluctuations is outside the inertial subrange of turbulence. Several theories have been developed to explain the nature of these echoes. For an excellent background on PMSE and proposed theories, see Cho and Röttger (1997), Rapp (2000), and Rapp et al. (2003).

Observational data have shown that polar mesosphere summer echoes sometimes exhibit layers with thicknesses less than 100 m (Chilson et al., 2001; Franke et al., 1992). Several theories have been proposed to explain the small-scale vertical layering observed in PMSE. For example, Havnes et al. (1992) have proposed that the observed structure of PMSE is explained by dust-hole scatter, where horizontal vortex rolls are embedded in a field of falling charged dust or ice aerosols. It is assumed that the core of the vortex has no aerosols leading to sharp gradients in the aerosol density at the boundaries. Another theory proposes that the observed structure, often exhibiting more than two layers, is due to gravity wave modulation of the background temper-

ature profile (Chilson et al., 1997; Rapp et al., 2002). Unfortunately, conventional radars used to observe PMSE are typically limited to 150-m range resolution. Therefore, it is imperative to employ new techniques, like interferometry, to obtain better resolution. Interferometry allows higher resolution capabilities than standard radar techniques and at the same time allows the use of new adaptive spectral estimation methods such as Capon.

In order to study the fine-scale PMSE vertical structure, an experiment was conducted in Tromsø, Norway (69.6° N, 19.2° E) using the European Incoherent SCATter (EISCAT) VHF radar in a Range IMaging (RIM) mode. RIM offers the power of studying small-scale vertical structure within a single sampling volume and is dependent upon the use of several carrier frequencies (Palmer et al., 1999; Luce et al., 2001). By proper phase shifting, these frequencies can be aligned, providing constructive interference at a particular range of interest. Therefore, when performing RIM, it is necessary to know the phase differences between the transmitter and receiver signals in order to choose proper shifts among the signals. Due to the design of the EISCAT receiver system, the transmitter and receiver do not have the same initial phase. This design introduces unavoidable and unknown phase errors that degrade the resulting range images.

RIM has many similarities to Coherent Radar Imaging (CRI), which is used to image in angle using several spatially separated receivers (Kudeki and Sürücü, 1991; Hysell, 1996). Since spatially separated receivers are typically part of an existing calibrated phased array radar system, phase calibration issues do not arise. However, when the array sizes become large or the system is susceptible to large variations in phase, calibration can be necessary. For example, similar phase calibration issues are found in the field of radio astronomy imaging when spatial interferometry is performed. Phase instabilities caused by instrumentation and/or atmospheric effects degrade the retrieved images. Several methods have been developed to alleviate this problem. Phase closure (Cornwell, 1989) is one of the first methods used in radio astronomy to correct images. In this method, a minimum of three evenly spaced antennas is required. The simplicity of this method relies on the principle that for any given antenna, phase errors canceled in the sum of the phases around a given loop of receivers. However, the major problem with this method is that one phase difference must be known to solve for the other phase differences and form the spatial covariance matrix.

A widely used imaging method in radio astronomy is the CLEAN algorithm (Cornwell et al., 1999). This method is an iterative algorithm which deconvolves a sampling function (dirty beam) from an observed brightness (dirty map) of a radio source. The CLEAN algorithm has been combined with phase closure to form the so-called self-calibration technique (Cornwell and Fomalont, 1999). This method is fundamentally a recursive model fitting, combining CLEAN with a phase closure relationship which is relevant due to the correlation between antennas. Since no explicit phase error values are provided by CLEAN, the application of self-calibration

to RIM is problematic. More recently, Friedman (2001) used genetic algorithms (GA) to enhance radio astronomy images. GA is a multi-dimensional optimization technique based on natural principles which uses a fitness function to evaluate each new potential solution. Through computer simulations, he found that by using the image sharpness as a fitness function, restored images of a point radio source showed considerable improvements.

In the present work and following the concepts of Friedman (2001), a novel method based on the GA, which uses the Fourier RIM imaged power in a predefined image window as the fitness function, is proposed to mitigate phase errors. A correction matrix is estimated using these phase errors retrieved from the GA process and is assumed to be time invariant throughout the image. It will be shown through computer simulations that this method retrieves enhanced RIM PMSE images in the case of both evenly and unevenly spaced frequencies. Subsequently, the calibration method was applied to preliminary data from the EISCAT experiment, thus providing the first results of RIM images of PMSE.

In Sect. 2, the radar configuration for the 2002 PMSE campaign using the EISCAT VHF radar is presented. In Sect. 3, the major problem statement is presented and the effects of phase errors on the RIM technique are discussed. A brief introduction to genetic algorithms and the proposed phase calibration method are described in Sect. 4. In Sect. 5, a numerical model is discussed that has been used to simulate atmospheric echoes within several sampling volumes. Simulation results using this model and the proposed phase calibration method are presented. Furthermore, preliminary experimental results from the EISCAT VHF radar are presented in this section. Finally, conclusions are provided in Sect. 6.

2 Experiment

The EISCAT VHF radar has a nominal operating frequency of 224 MHz, but it is capable of operating at frequencies ranging from 222.4–225.4 MHz in steps of 200 kHz. The 16 possible frequencies are denoted by F0–F15, respectively. An individual receiver is required for each frequency used and, at the time of the experiment, five receiver boards were available. During the design of the experiment, many combinations of the five possible frequencies were used in search for the optimal combination. Sidelobe suppression and mainlobe width in the Fourier range pattern were a trade-off in the search for this optimal combination. Although somewhat ad hoc, we have chosen a frequency set which results in a narrow main lobe, relatively small sidelobes, and well separated grating lobes. For the preliminary results presented here, the frequency combination, F7, F9, F11, F13, and F15, was used, providing a 400-kHz frequency sampling and 375-m grating lobe separation.

The radar transmitted and received on five alternating frequencies. In our experiment, data were collected for an altitude range of 72.0–101.7 km with 100 range-gated sampling volumes (hereafter called range gates) and a 300-m range res-

Table 1. Significant radar parameters.

Parameter	Setting
Frequencies (MHz)	F7 F9 F11 F13 F15 223.8 224.2 224.6 225.0 225.4
Sub-pulse length	2 μ s
Range resolution	300 m
Code	64-bit complementary code
Code sequence	A \bar{B} A B
Effective IPP	8.68 ms
Aliasing velocity	9.62 ms ⁻¹
Beamwidth	0.64° (zonal), 1.92° (meridional)
Time-series points	144 (per frequency)
Range gates	100

olution. A 64-baud complementary code sequence was used, and pulses were transmitted with an inter-pulse period (IPP) of 1.736 ms. Using the five frequencies, the effective inter-pulse period was 8.68 ms. For each of the five frequencies, 144 complex time-series points were collected. The sub-pulse length was set to 2 μ s with a 500 kHz bandwidth for the transmitted pulse. Therefore, the total bandwidth for the five frequencies was 2.1 MHz. In the case of Fourier RIM, a range resolution of 60 m is expected when using five frequencies. Furthermore, RIM easily allows the use of higher-resolution algorithms such as the Capon method (Palmer et al., 1999).

The EISCAT VHF antenna is a partial parabolic cylinder extending over 120 m and 40 m in the zonal and meridional directions, respectively. Therefore, the beamwidth is not symmetric and has two-way, half-power beamwidths of 0.6° and 1.7°, in the zonal and meridional directions, respectively. The antenna gain is about 46 dBi and it was pointing vertically during the observations. At the nominal operating frequency of 224 MHz, the transmitter operates at about 1.5 MW peak power. A summary of the important parameters is provided in Table 1.

Figure 1 shows a simplified block diagram of the EISCAT digital receiver. Since the digital receivers operate at the lower frequency range of 8.4–11.4 MHz, received signals are down-converted using an oscillator that is phase locked to the transmitter by a Global Positioning System (GPS). However, the initial phases of the transmitter and receiver can be different, making the RIM implementation problematic.

After band-pass filtering, the digital receiver uses a Numerically Controlled Oscillator (NCO) to produce the base-band in-phase and quadrature (I and Q) signals. This digital oscillator introduces quantization errors due to its 32-bit frequency word. In the standard mode of the EISCAT VHF radar, these errors are negligible, since just one frequency is used ($\approx 2.9 \times 10^{-3}$ ms⁻¹ for F7). When signals from multiple frequencies are used for interferometry measurements, however, these errors can create significant phase errors. Fortunately, these quantization errors are deterministic and can be easily removed offline.

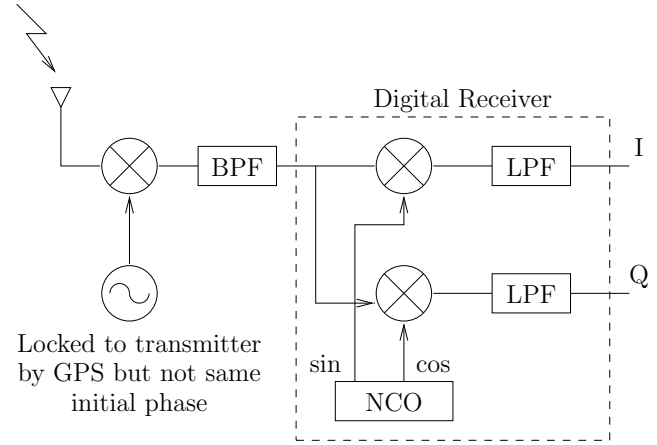


Fig. 1. Block diagram of the EISCAT VHF digital receiver system. BPF and LPF designate the band-pass and low-pass filters, respectively.

As discussed previously, the EISCAT VHF radar transmitter and receiver do not have the same initial phase. In the next section, a mathematical formulation of the consequences of this problem on range imaging is discussed.

3 Effect of phase errors on range imaging

We will now mathematically describe the signals used for RIM processing with the EISCAT VHF radar. The initial phase values for the transmitter and receiver using frequency n will be denoted by δ_T^n and δ_R^n , respectively. Assuming a single layer located at range z_I , the returned, coherently detected signal x_n can be modeled as the following

$$x_n = \tilde{A}_n e^{j[\omega_d^n t + \delta_n - 2k_n \tilde{z}]} + \epsilon_n, \quad (1)$$

where \tilde{A}_n is the returned complex amplitude and ω_d^n represents the Doppler frequency for frequency n . The term $\delta_n = \delta_T^n - \delta_R^n$ is the difference in the phase of the transmitter and receiver. The factor 2 is due to the two-way path of the traveling signal, k_n is the corresponding wave number for frequency n , and $\tilde{z} = z_I + z_0$ is the sum of the layer range (z_I) and the range shift due to the system delay (z_0). Finally, ϵ_n represents the additive white Gaussian noise in each signal with zero mean and variance σ^2 . It is assumed that the phase difference δ_n remains constant throughout the experiment.

In standard RIM analysis, the cross-covariance between all combinations of signals must be calculated in order to construct the covariance matrix \mathbf{R} . By definition, the cross-covariance between two signals l and m can be written as

$$R_{lm} = \langle x_l x_m^* \rangle, \quad (2)$$

where $\langle \cdot \rangle$ is the expected value operator and $*$ represents the Hermitian operator. Assuming that noise from different receivers are uncorrelated, and that variations in Doppler

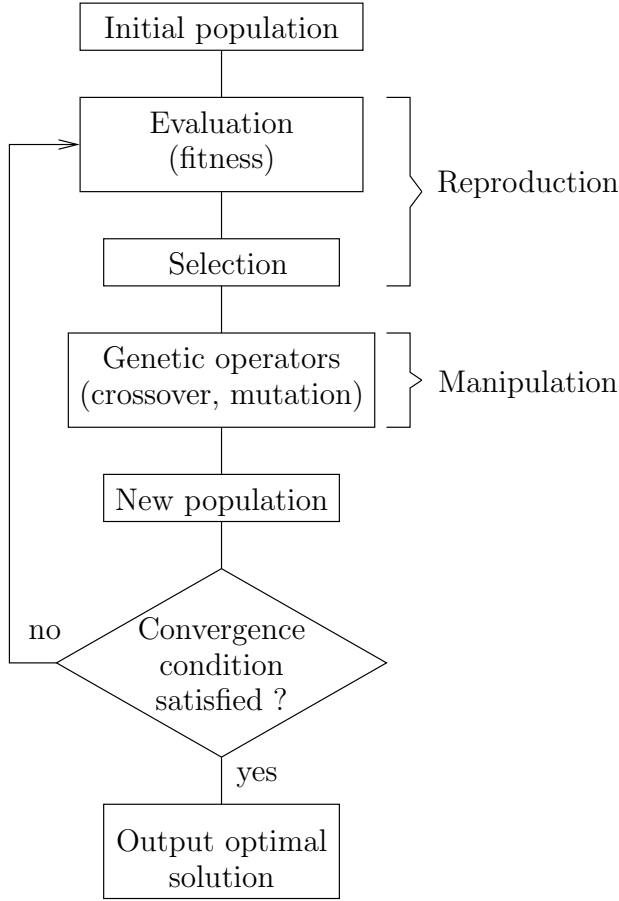


Fig. 2. Simple genetic algorithm (SGA) structure.

shift across the independent frequencies are small, the cross-covariance can be approximated by

$$R_{lm} = \langle \tilde{A}_l \tilde{A}_m^* \rangle e^{j\hat{\delta}_{lm}} e^{-j2z_l(k_l - k_m)} + \sigma^2 \delta(l - m), \quad (3)$$

where $\delta(l - m)$ is the Kronecker delta function. The $\hat{\delta}_{lm}$ term involving the initial phase differences, and the unknown range shift due to the system delay is given by

$$\hat{\delta}_{lm} = (\delta_l - \delta_m) - 2z_0(k_l - k_m). \quad (4)$$

The second exponential term in Eq. (3) provides the information about the range of the atmospheric layer.

Using standard coherent demodulation techniques with RIM, the initial phases will be the same, thus simplifying the processing. For that case, the $\hat{\delta}_{lm}$ will depend only on z_0 . Furthermore, if z_0 is assumed to be known through a system delay calibration, $\hat{\delta}_{lm} = 0$. Therefore, phase calibration would not be necessary and Eq. (3) would be reduced to

$$R_{lm} = \langle \tilde{A}_l \tilde{A}_m^* \rangle e^{-j2z_l(k_l - k_m)} + \sigma^2 \delta(l - m). \quad (5)$$

Assuming a constant phase offset between the transmitter and receiver, the covariance matrix \mathbf{R} can be obtained by using Eq. (3) for all possible combinations among the N fre-

quencies. As stated by Palmer et al. (1999), the Fourier RIM power profile $P_F(r)$ is given by

$$P_F(r) = \mathbf{e}^*(r) \mathbf{R} \mathbf{e}(r) / N^2, \quad (6)$$

where $\mathbf{e}(r) = [e^{-j2k_1 r} e^{-j2k_2 r} \dots e^{-j2k_N r}]^T$ is the range steering vector and T represents the transpose operator. The range values r within a range gate are called subgates and can be adjusted to obtain better sampling within the volume. There is no limitation in the number of subgates. However, the inherent resolution depends on the total bandwidth and the algorithm used to estimate the power profile.

By substituting Eq. (3) into Eq. (6) and assuming one layer located at z_l , it can be shown that the Fourier RIM power is given by

$$P_F(r) = \sum_{i=1}^N \frac{\langle |\tilde{A}_i|^2 \rangle + \sigma^2}{N^2} + \frac{2}{N^2} \sum_{n=1}^{N-1} \sum_{m=n+1}^N \langle \tilde{A}_n \tilde{A}_m^* \rangle \cos \alpha_{nm} \quad (7)$$

and

$$\alpha_{nm} = 2(k_n - k_m)(r - z_l) + \hat{\delta}_{nm}, \quad (8)$$

The term $\hat{\delta}_{nm}$ represents the phase errors given in Eq. (4). As seen, these phase errors introduce a phase shift for each cosine function in the summation of the Fourier power within a given range gate. The first term in Eq. (4) alone introduces a defocusing effect in the image within a given gate since it is random in nature. In contrast, the second term introduces a shift in the overall image within a given gate. Both sources of error decrease the overall power. If no errors are present, the cosine functions will be aligned at the imaged range z_l and will add coherently.

Additional resolving power and interference rejection capabilities are possible using RIM based on the Capon spectral estimation method (Palmer et al., 1999). In this case, the RIM power profile is given by

$$P_C(r) = \frac{N + 1}{\mathbf{e}^*(r) \mathbf{R}^{-1} \mathbf{e}(r)} \quad (9)$$

where the numerator is an approximation of the Capon filter bandwidth needed to produce an estimate of the power spectral density (Stoica and Moses, 1997). Since a matrix inversion is involved in the equation, robustness issues may arise. In rare conditions, the covariance matrix \mathbf{R} may become close to singular when phase errors are present.

From the previous analysis, it is obvious that proper calibration is important for experiments using the RIM technique. In the next section, a new calibration method to solve for these phase errors is described. This novel calibration method is based on genetic algorithms and uses the Fourier RIM power as an evaluation function to solve for the optimal solution. Since a matrix inverse is required for Capon RIM, this technique is not used as an evaluation function in the calibration algorithm. However, it will be used after phase calibration to produce the final imaging results.

4 Phase calibration using genetic algorithms

4.1 The simple genetic algorithm

Genetic algorithms (GA) are a robust optimization technique based on natural evolutionary mechanisms. This method was first introduced by Holland (1975) and since that time, has become a practical, robust optimization and search technique. The first GA algorithm was called the Simple Genetic Algorithm (SGA) with the goal of obtaining better estimates in global optimization scenarios. SGA mimics nature’s evolutionary characteristics by manipulating a given population of possible solutions (individuals), and searching for the best solution to solve an optimization problem. Basically, SGA operates through the following steps:

- creation of a population (possible solutions),
- evaluation of each individual in the population,
- selection of the best individuals,
- genetic manipulation to create a new population.

Figure 2 shows these four basic steps in the SGA flow-chart structure. Initially, a population of possible solutions is randomly generated within a certain range of predefined values, depending upon the problem to be solved. These solutions (individuals) are usually encoded using a binary alphabet. For example, if the minimum of the function $f(x)=x^2$ is desired, a population of possible solutions could be generated over the interval $-10 \leq x < 10$. Each individual is then encoded using a binary alphabet. That is, if an individual value is 9, then its binary representation using 1’s and 0’s is given by 1001 in the case of a four-bit word. The string of bits resembles the chromosomes of each individual in nature.

Applying the natural selection principle, every possible solution is associated with a fitness value that indicates the optimality of the solution. The higher the fitness value, the higher the possibilities of survival in future generations. In order to assign fitness values to the members of a population, a fitness function should be defined. This function is used as a discriminator to evaluate each string in the SGA process, and its formulation depends on the optimization problem to be solved. In the given example, the function $f(x)$ is used as a fitness function to evaluate each individual. Then fitness values are assigned to each individual. Since we are minimizing, individuals with lower function values are assigned higher fitness values.

Once fitness values are assigned, a selection mechanism is established to create a pool of individuals that are allowed to reproduce in future generations. In this step, N individuals are selected to be strongest by assigning them a specific number of offspring. In our approach, the selection scheme is performed by stochastic universal sampling selection (Barker, 1987). According to this scheme, each individual is assigned to a sector of a circle (wheel) with its total angular span proportional to its fitness value. Then, N equally spaced markers are placed around the circle. The wheel is spun once and

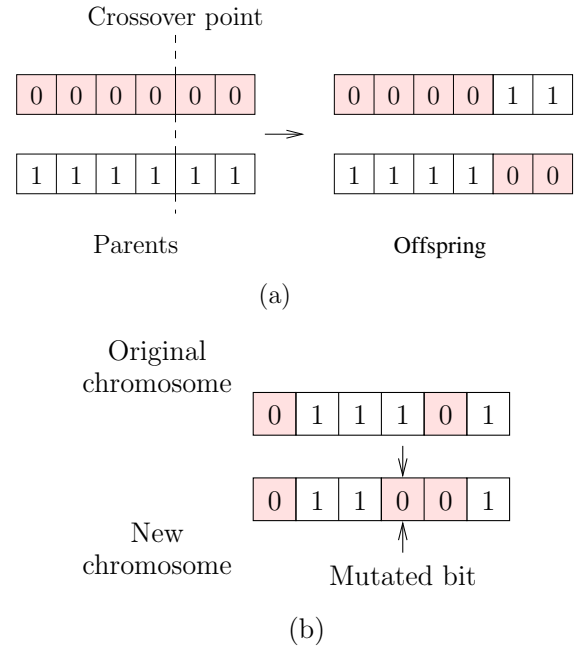


Fig. 3. Manipulation operations. (a) Crossover. (b) Mutation.

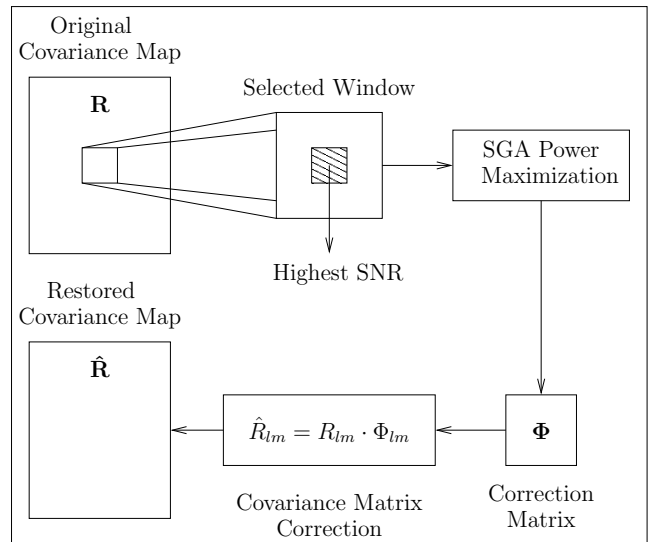


Fig. 4. Proposed phase calibration method.

all individuals (sectors) that fall close-by to a marker are selected. That is, depending on the sector assignment, more than one marker could fall in the same sector. Consequently, higher fitness individuals have a higher probability to reproduce.

After selection, parents are chosen randomly to be manipulated. The manipulation process involves two genetic operators called crossover and mutation. At this stage, a new population of individuals is produced by manipulating the “genetic information” inherent to each parent. This genetic information is represented by its binary string or encoded representation. In the crossover operation, two parameters

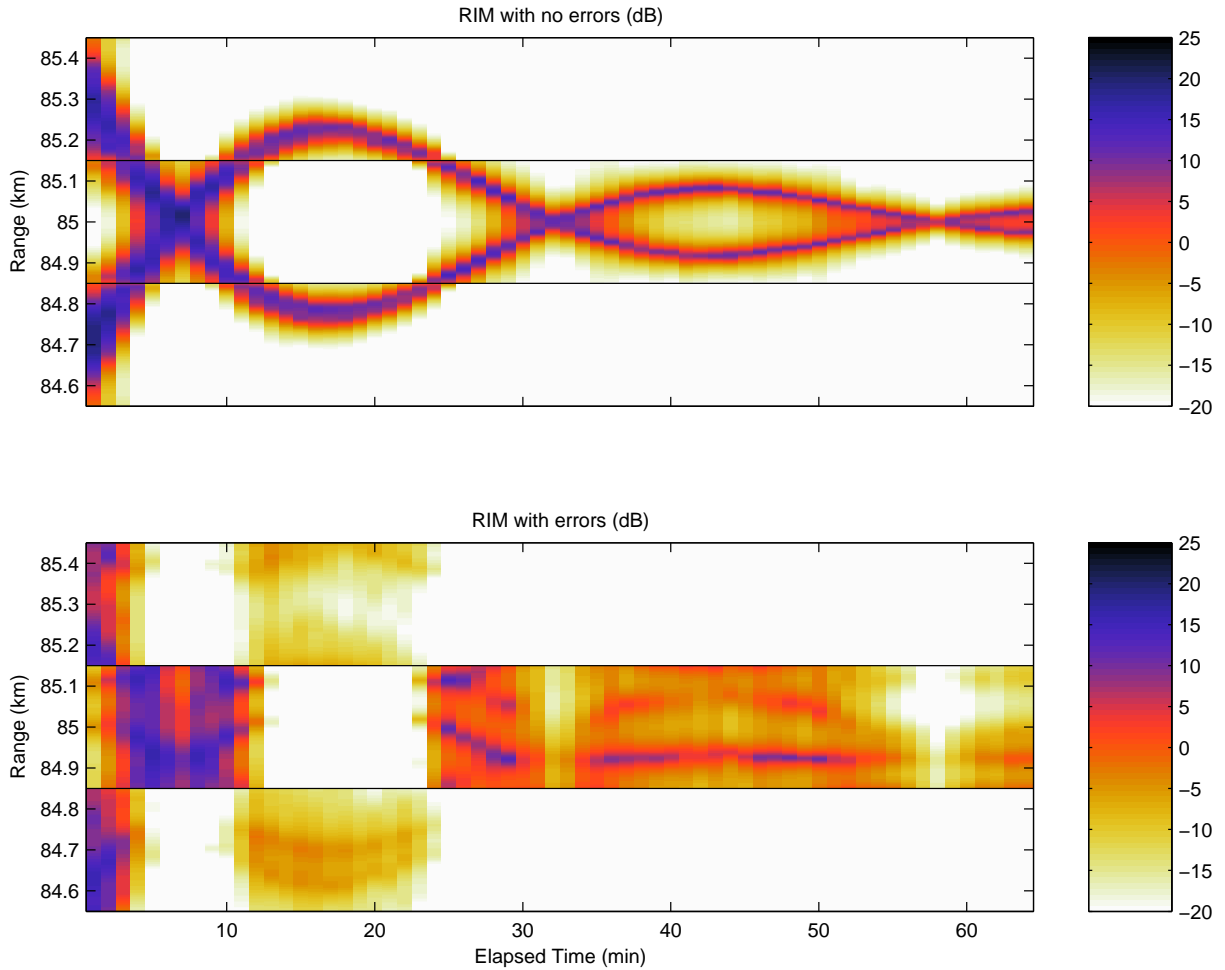


Fig. 5. Capon RIM image without phase error and infinite SNR is shown in the top panel. After inclusion of randomly chosen, but constant, phase errors, the image is severely distorted and is provided in the bottom panel.

should be defined previously: crossover points and crossover rate. Crossover points are points where strings are swapped to produce a new string, as depicted in Fig. 3a. They divide the original string into several pieces that are interchanged in the crossover operation. SGA uses a single crossover point and it is randomly allocated. The crossover rate is a predefined number between 0 and 1 and dictates when the crossover operation takes place. When two parents are chosen to reproduce, a random number between 0 and 1 is generated, and if it is greater than the crossover rate, then the crossover operation is executed and the parents are replaced in the population by their offspring. Otherwise, parents are preserved for the next generation. In summary, the crossover operation allows the genetic information of two parents to be interchanged by swapping part of their binary strings at the crossover point.

In the mutation operation, a random single bit from a string is complemented. Figure 3b shows the mutation operation applied to the fourth element of the string. Mutation involves restoration of the genetic material which possibly can be lost in the SGA process. For example, suppose that in a given

bit position, all strings of a population have converged to a 0 and the optimal solution has a 1 in that position. As a result, crossover alone cannot modify that particular bit. However, by using mutation, this bit restoration can be reached efficiently. Similar to crossover, mutation only takes place when the so-called mutation rate is exceeded. This probability of mutation should be defined previously in the SGA algorithm.

Therefore, after manipulation, a new population is produced with more optimal genetic characteristics. The SGA repeats the cycle until a certain condition is satisfied. This condition could be, for example, a predefined number of generations or some desired fitness level.

4.2 Proposed phase calibration algorithm

Using the SGA principles described, a phase calibration algorithm is devised to search for the unknown phase errors introduced in the covariance matrix. As shown in Sect. 3, phase errors produce unfocused RIM images within each range gate. As a result of this defocusing, the overall RIM power is decreased according to Eq. (7). If no errors are as-

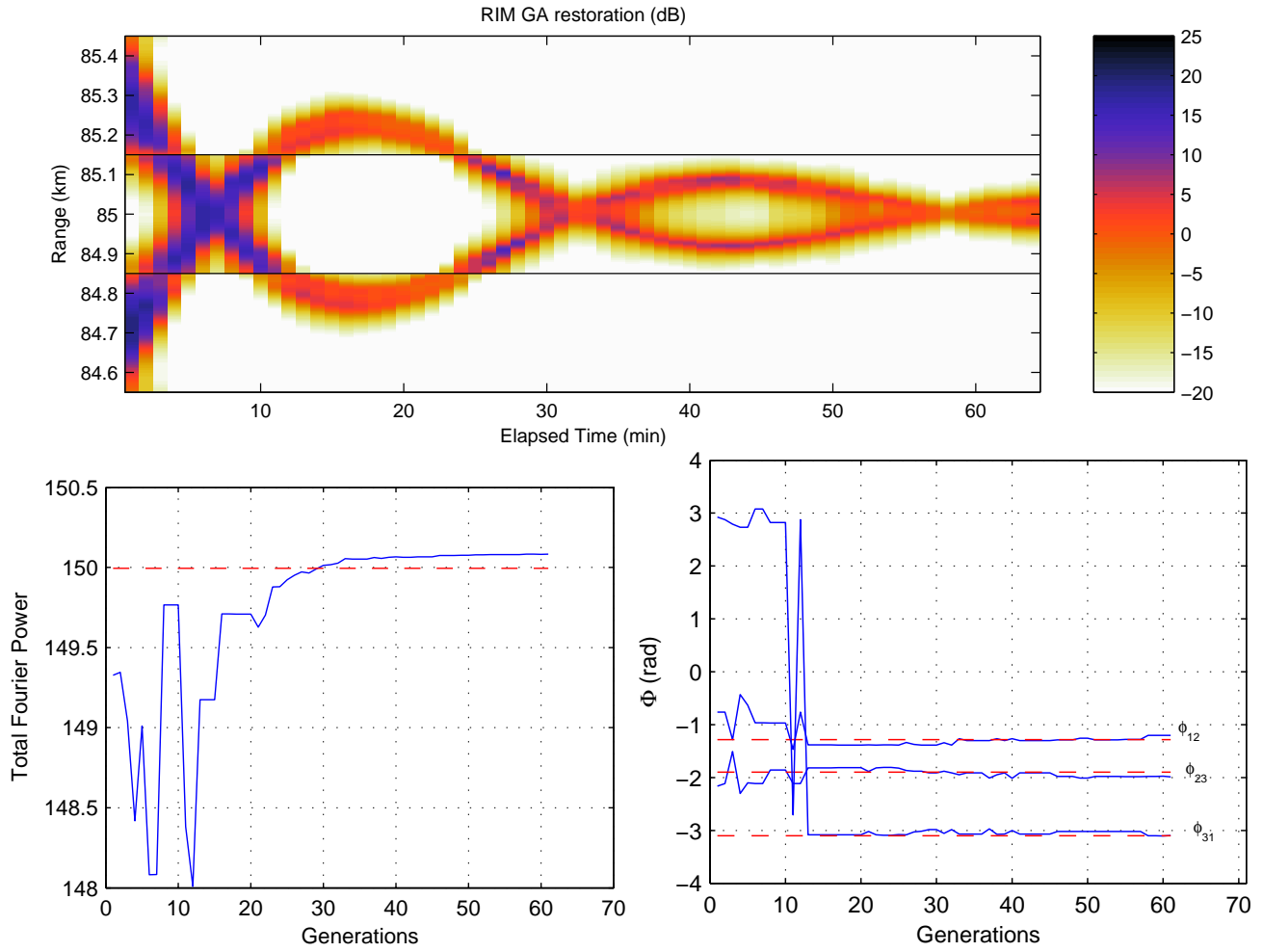


Fig. 6. Capon restored RIM image using the GA-based phase calibration method (top panel). The convergence is observed in both the total Fourier power (fitness) and the estimated phase values shown in the bottom panel.

sumed, the total power would be maximized and can therefore be used as a fitness function for the SGA.

A schematic of the proposed calibration method is depicted in Fig. 4. First, the covariance matrix for each time and range (pixel) is estimated. Therefore, the original covariance matrix map containing phase errors can be formed. Consequently, conventional range-time-intensity (RTI) maps of the power and signal-to-noise ratio (SNR) are generated averaging all frequencies. Power RTI maps can be obtained by averaging the diagonal values of \mathbf{R} at each pixel. From the power RTI maps, SNR RTI maps are constructed for each time, assuming that a certain height contains no atmospheric return and can therefore be used to estimate noise power. Then, a predefined window in the covariance matrix map is chosen as the region surrounding the highest SNR pixel. It should be emphasized that RTI maps are only used as a reference to obtain the highest SNR pixel and therefore to establish a predefined window in the covariance matrix map. The specific limits of range and time defining the window region are set by the user. A larger window allows better horizontal

and vertical continuity of pixels but is computationally limiting.

In the selected window, the SGA algorithm is applied according to the process described in Fig. 2. In this case, the total Fourier RIM power is taken as an evaluation function to be maximized. Since covariance matrices are known, Fourier RIM power can be estimated for each pixel using Eq. (6). Therefore, the total Fourier RIM power is obtained by summing the Fourier RIM power of all pixels within the predefined window. As stated in Eq. (1), unknown phase values for each frequency can be defined as

$$\phi_l \equiv \delta_l - 2z_0 k_l, \quad (10)$$

where $l=1, \dots, N$. Accordingly, these phase errors form the undesired phase offset in the covariance matrix elements given by

$$\delta_{lm} = \phi_l - \phi_m. \quad (11)$$

Initially, a population of phase values (ϕ_l^i) ranging from $0-2\pi$ is randomly generated. Since we are using N fre-

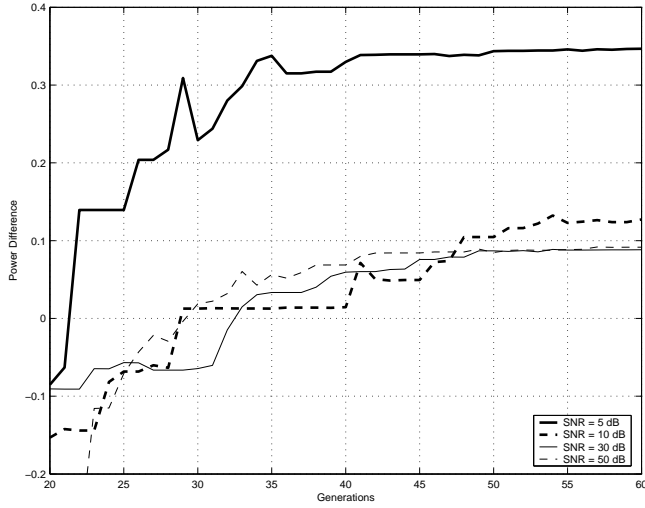


Fig. 7. Fourier power difference convergence for different SNR scenarios. Fourier power difference is obtained by subtracting the total Fourier power for each generation from the total Fourier power without errors.

quencies, every individual i is described by N phase values encoded with a specified number of bits per frequency.

When the fitness function is called for an evaluation, a unique phase calibration matrix denoted by Φ^i for a specific individual i is formed according to Eq. (11) with the following elements

$$\Phi_{lm}^i = e^{-j\delta_{lm}^i}, \quad (12)$$

where l and m represent the different frequency combinations ($l, m=1, \dots, N$). If $\delta_{lm}^i \approx \hat{\delta}_{lm}^i$, the total Fourier RIM power will be maximized and the term Φ_{lm}^i is chosen so as to cancel the original phase offsets.

Recall that $\hat{\delta}_{lm}^i$ was given in Eq. (4) and includes initial phases and system delay. Then, the calibration operation is simply performed by an element-by-element multiplication of the contaminated covariance matrix with calibration matrix $\hat{R}_{lm} = R_{lm} \cdot \Phi_{lm}^i$ at every evaluation. The selection algorithm assigns high fitness values to individuals that allow the total Fourier RIM power to be maximized. The SGA loop is repeated until a certain number of generations is reached. After the SGA process, the optimal phase calibration matrix Φ is formed and used to create the entire RIM image using any desired algorithm.

It should be emphasized that there is no restriction related to the frequency spacings in the proposed phase calibration algorithm, since Fourier RIM is applied using Eq. (6). Further, the number of subgates or range sampling in the fitness function is not limited. A large number of subgates per range gate will ensure better estimation of the fitness function and thus better SGA performance. However, choosing a larger window and a larger number of subgates increases the SGA computational burden.

In the next sections, the proposed phase calibration method will be used with both actual and simulated data from the EISCAT radar.

5 Results

5.1 Numerical simulation results

Numerical simulations have been used to verify the proposed GA-based phase calibration technique. The simulation method is based on the atmospheric model originally proposed by Holdsworth and Reid (1995). The model assumes a three-dimensional field of point scatterers randomly located within an enclosing volume. As time progresses, the scatterers follow a predefined mean flow and a spatially correlated turbulent flow. As scatterers leave the volume, new scatterers are inserted in the opposite position. In this way, the total number of scatterers is kept constant. Using a table look-up method in lieu of a cumbersome three-dimensional spatial filter to create spatially correlated turbulent flow, Cheong et al. (2003) have recently modified the method allowing thousands of simulated scatterers with little computational burden. Nevertheless, in order to mimic layering structure continuity across gates, a novel RIM simulation was implemented by creating a set of range-separated range weighting functions within the enclosing volume.

For the purpose of matching the EISCAT experiments, a set of five evenly spaced frequencies were used – F7, F9, F11, F13, and F15, as defined in Table 1. Using 1000 randomly distributed scatterers, 64 records of 128 time series points corresponding to the I and Q radar outputs were generated for three range gates. The center range gate was located at 85 km and the range resolution was set to 300 m. Two overlapping sinusoidal layers were simulated with amplitudes such that the structure crossed the three simulated range gate boundaries. Figure 5 shows the Capon RIM image without (upper panel) and with (lower panel) random phase errors for an infinite SNR and 128 subgates per range gate. In our simulations, random phase errors (ϕ_l), defined in Eq. (10), are introduced in the time series for each frequency. As can be seen, these phase errors severely degrade the resulting RIM image. Obviously, phase errors of this magnitude could never be tolerated for proper interpretation of the data. As pointed out earlier, phase errors (ϕ_l) are due to transmitter-receiver phase differences and system delay errors. Both sources of error are compensated using the proposed calibration method. As a result, our method follows a general approach in the sense that any phase error can be included in ϕ_l and the calibration procedure will attempt to mitigate the effects. The only requirement is that the phase errors should be constant throughout the experiment. Since all phase errors are incorporated into our simulations, the image degradation analysis due to phase errors studied in Palmer et al. (1999) is applicable to our case.

Subsequently, the proposed phase calibration method described in the previous section was applied to the corrupted

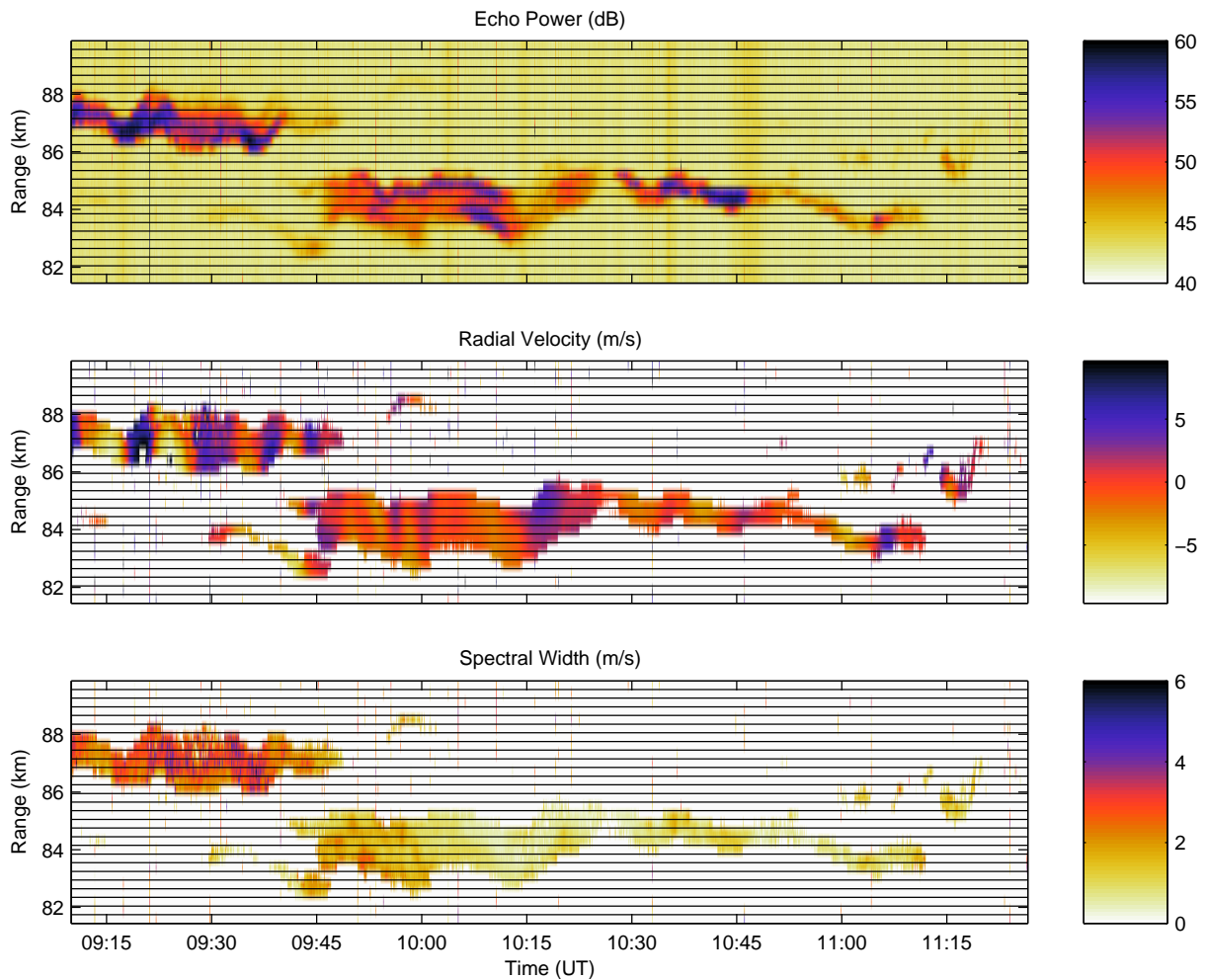


Fig. 8. Time histories of standard echo power, radial velocity, and spectral width from the observed PMSE on 30 July 2002.

synthetic data. A population size of 100 individuals was randomly generated. Each individual is represented by five phase values ranging from $0-2\pi$ with a 20-bit word. A crossover rate of 0.7 and a mutation rate of 0.007 were chosen. Furthermore, 60 generations and a window that covers the entire image was used. These GA values were chosen empirically, although the results are not particularly sensitive to these parameters. For the fitness function, Fourier RIM was performed for each generation using 32 subgates. Figure 6 shows the Capon SGA restored image in the upper panel, as well as the convergence behavior of the total power and three representative phase difference components of the covariance matrix in the lower panels. For comparison, 128 subgates per range gate were chosen when displaying the final RIM restored image.

The restored RIM image shows good agreement with the original image shown in the upper panel of Fig. 5. Furthermore, it is shown that 60 generations are sufficient to achieve power and phase error convergence for this particular case. Red dashed lines indicate the model values in the lower panels. It can be seen that the total Fourier power of the image without errors is less than the estimated one. This indicates that a quantized total Fourier power is maximized, depend-

ing on the number of subgates used in the fitness function. As stated previously, better estimates can be obtained using more subgates at a computational cost. In the right lower panel, three of the estimated phase values of the Φ matrix are provided showing convergence to the model values.

Figure 7 shows the proposed phase calibration algorithm performance for different SNR. In this plot, convergence of the total Fourier power difference is shown as a function of the number of generations. The Fourier power difference is obtained by subtracting the total Fourier power for each generation from the total Fourier power without errors. It is desired to have a small power difference. Convergence rates are similar except in the case of extremely low SNR of 5 dB. Although the convergence rate may seem relatively fast, for this case, the power difference is comparably large, exemplifying a poor calibration.

According to previous results, the proposed phase calibration method is capable of removing phase errors from the simulated data. Next, real data collected during the July 2002 EISCAT campaign will be examined. To facilitate comparison, the same SGA parameters used in the simulation will be used for the experimental data.

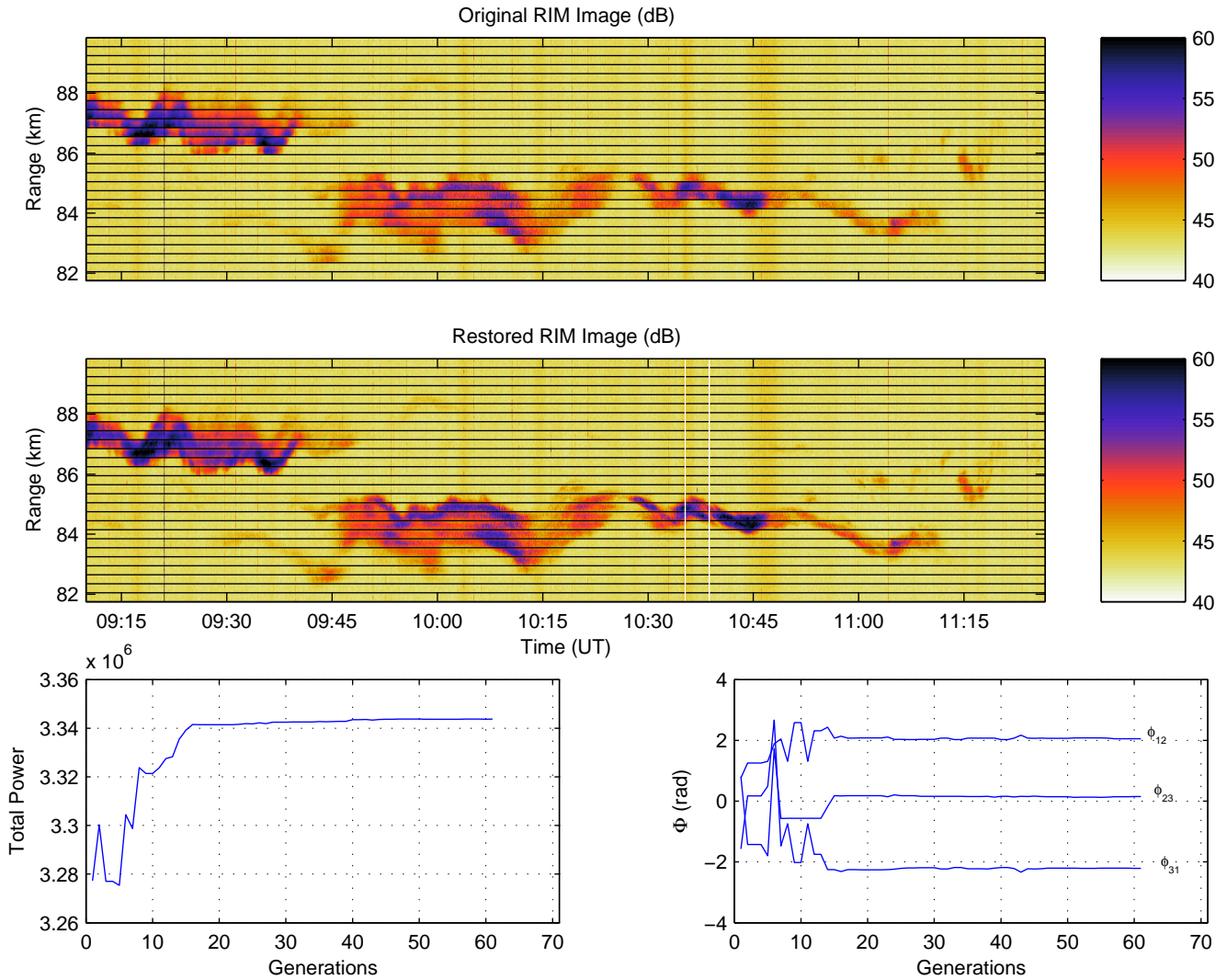


Fig. 9. Comparison of corrupted RIM image and phase-calibrated RIM image. Learning curves and convergence rates are observed in the bottom panels of the figure.

5.2 Experimental results

In this section, experimental data results collected in the 2002 EISCAT PMSE campaign are presented. An approximate two-hour period on 30 July 2002, is analyzed using the pulse pair processor technique (e.g. Doviak and Zrnić, 1993). Subsequently, the proposed phase calibration technique is used to mitigate phase errors on the RIM images obtained using the same data. Later, physical descriptions of the first calibrated RIM PMSE images are provided.

As mentioned in Sect. 2, the experiment used five frequencies – F7, F9, F11, F13, and F15, as provided in Table 1. A total of 100 range gates with a range resolution of 300 m was employed. For complete information about the experiment, the reader is referred to Table 1. Figure 8 shows the general morphology of the observed PMSE over an approximate two-hour period. Using standard correlation-based processing techniques, the echo power, radial velocity (approximate

vertical velocity) and spectral width are provided in the figure. The data were estimated using the average of the five frequencies to reduce statistical variation. For the case of radial velocities and spectral widths, only pixels having a corresponding SNR above a -5 dB threshold are shown to ensure that the data were not biased by noise. Displayed vertical velocity values are shown within the aliasing velocity range of $\pm 9.62 \text{ ms}^{-1}$.

A typical double-layer structure is seen in the echo power plot with the upper layer at 87 km diminishing as the lower layer appears at 84 km. The vertical velocity exhibits a distinct monochromatic wave structure with an apparent period of approximately 10 min. The sign of the vertical velocity, toward (negative) or away (positive) from the radar, is clearly correlated with the apparent motion of the layers in the echo power plot. The spectral width measurements point to higher stability in the lower layer. Such conclusions have also been seen by other researchers (Cho et al., 1993; Lübken et al.,

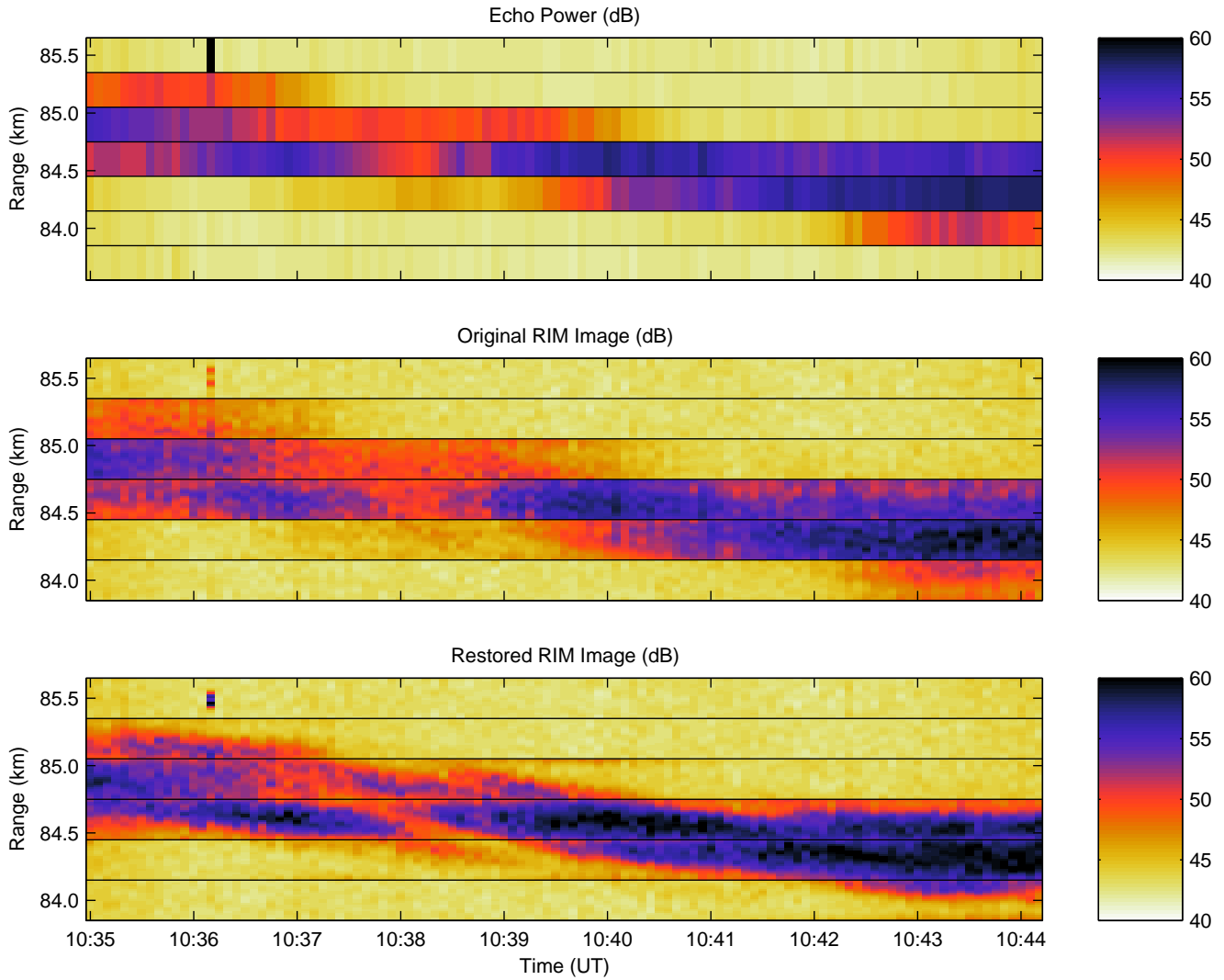


Fig. 10. Smaller region of the overall data set. Echo power, corrupted RIM image, and phase-calibrated RIM image are shown in the figure.

1993; Czechowsky and Rüster, 1997; Chilson et al., 2001). It should be noted that due to the narrow beamwidth of the EISCAT VHF radar, any beam-broadening effects on the spectral width estimates are insignificant (Hocking and Röttger, 1997).

The previous figure provided results from standard processing without using the capabilities of the multiple frequency experiment. We will use the RIM method to enhance the fine detail assumed to be present in the structure of the PMSE. Although Capon RIM results are presented in this section, it should be noted that at least a 60-m range resolution is expected from Capon RIM processing. Due to the adaptive nature of the Capon algorithm, its resolution is difficult to define. However, previous work has shown the Capon method to possess approximately twice the resolution capabilities of Fourier (Palmer et al., 1999; Chilson et al., 2003).

Figure 9 shows a comparison of the corrupted Capon RIM power image with random phase errors and the calibrated RIM image after the application of the proposed GA-based method. The same SGA parameters used in the simulation

section were applied in the real data phase calibration. However, 16 subgates were used in the fitness function and 20 subgates used for display purposes.

The vertical white lines at approximately 10:35 UT emphasize the region to which the calibration procedure was applied. The learning curves from the GA are also provided in the bottom panels of the figure. Given the large vertical extent of the PMSE layers, any enhancement due to the calibration is difficult to observe.

The effect of the GA-based calibration is more easily observed by scrutinizing a smaller region of the data. Figure 10 provides the echo power, original RIM image, and calibrated RIM image for a 10-min period from 10:35–10:45 UT at an altitude of approximately 85 km. Note the more natural transitions between range gates and finer detail in the calibrated RIM image. Further, range weighting-function effects can be observed similar to those reported by Chilson et al. (2003). Without calibration, the RIM power centers are distorted and unnaturally contained within each gate.

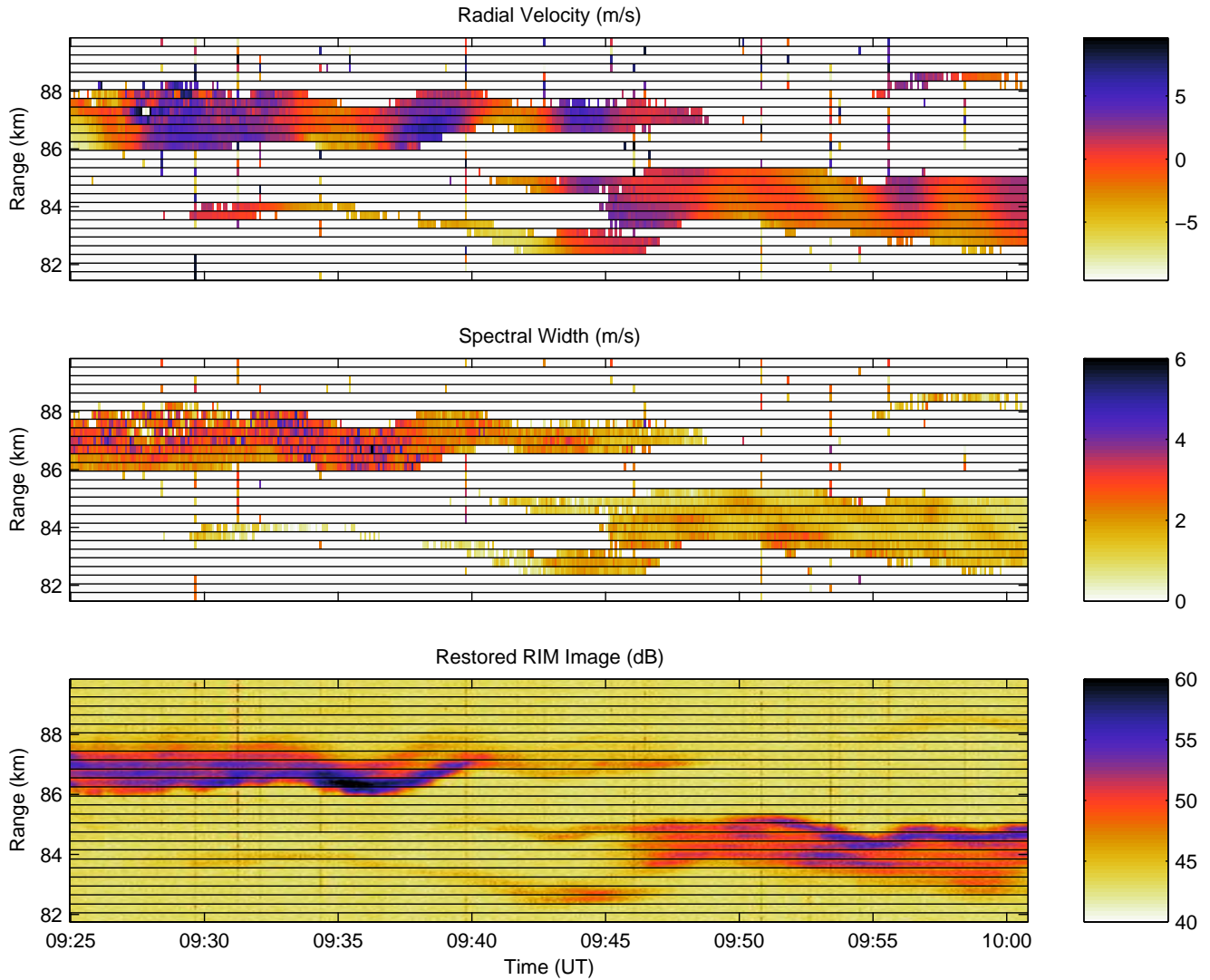


Fig. 11. Radial velocity (vertical), spectral width, and calibrated RIM image for a 35-min period centered at 85 km.

A specific RIM PMSE case study is depicted in Fig. 11. This particular data window was chosen since it exhibits significant vertical structure emphasizing the transition between the upper and lower layers. It was taken from the restored RIM image presented in Fig. 9. The radial velocity (vertical), spectral width, and calibrated RIM image are shown for a 35-min period and a 7-km region centered at 85 km.

An interesting effect is present in the multiple layers of the overall PMSE structure in that the vertical velocity shows vertical continuity throughout the layers. Therefore, it seems obvious that the multiple layers are dynamically connected, through at least the vertical flow, even though the echo power shows a distinct separation between the layers. The spectral width, which is related to aspect sensitivity, exhibits the expected behavior, where the lower layer at 84 km shows a significantly smaller spectral width than does the upper layer.

More interestingly, the upper layer at 87 km seems to show a similar effect up to about 09:34 UT, where the bottom side of the layer has smaller spectral width, mimicking the be-

havior of the overall layer. The RIM images can be thought of as high-resolution images of echo power and indicate an almost complete separation between the layers. The small-scale sub-layers possess a natural oscillation and transition between range gates indicative of gravity waves. The period is approximately 5–10 min with direct correlation with the vertical velocity structure. Given the vertical continuity of vertical velocity and the observed gravity wave activity, the multiple layering structure of the PMSE is more easily interpreted as due to gravity wave modulation of the background temperature profile (Chilson et al., 1997; Rapp et al., 2002). Generally, we find that the GA-based phase calibration method has allowed the calculation of RIM echo power images with improved resolution and clarity.

6 Conclusions

A novel GA-based phase calibration algorithm for RIM imaging applications has been presented. Using a new multiple range gate numerical simulation method, it was shown that this method provides robust initial phase estimation with fast convergence rates. The total power over a predefined window in the initial RIM image was used as the fitness function. By maximizing this total power as a function of phase error, the GA was able to provide convergent phase estimates within 10–20 generations. After obtaining the phase errors based only on the optimization of the predefined window, these errors could be applied to the entire image, reducing the overall computational burden. Preliminary PMSE images from the application of the RIM technique on the EISCAT radar were presented. Obvious image enhancement was obtained using the GA calibration method to reveal the fine-scale structure in the PMSE. Relationships among the vertical wind, spectral width, and the RIM structure were also made evident using the proposed calibration method.

Future studies should include the optimization of the GA with respect to the generation of the initial population. Simulated annealing and methods based on immune systems could provide a more optimal initial population increasing the GA convergence rates. Although not discussed in this work, it is also possible that the GA could be applied to the calibration of other imperfections in the data, such as, for example, amplitude and frequency variations.

The PMSE observations presented here reveal several features that have been previously reported in connection with PMSE. For example, our observations exhibit double-layer structures, which may be indicative of Kelvin-Helmholtz instabilities (KHI) (Hill et al., 1999). Further investigation of dynamical links to KHI necessitates height profiles of the horizontal wind field. We plan to examine these PMSE data in connection with wind observations obtained from the Ramfjordmoen MF radar (Hall, 2001) in a future study. It is unlikely, however, that much can be said about the topic of KHI, since the range resolution for the data collected with the Ramfjordmoen MF radar was only 3 km. Additionally, the widths of the Doppler spectra, which represent the variance in the line-of-sight velocity field, are larger in the upper portions of the echoing layers (Cho and Röttger, 1997). Broad spectral widths are only reported to occur in about 10–30% of all observations of PMSE (Lübken et al., 2002). In fact, a theory has recently been advanced by Rapp and Lübken (2003) where it is shown that PMSE can maintain plasma structures long after neutral air turbulence may have extinguished. The theory by Rapp and Lübken (2003) does not rule out other mechanisms, such as dust-hole scatter. Further investigation of these data and future PMSE data collected in a RIM mode could help address this topic.

Acknowledgements. J. R. F. and R. D. P. were supported by the Division of Atmospheric Sciences of the National Science Foundation through Grant ATM0122769. P. B. C. was supported by the Division of Atmospheric Sciences of the National Science Foundation through Grant ATM0123010. The authors thank G. Wannberg and

C. Heinselman for their technical assistance during the initial phase of this work.

The EISCAT Scientific Association is supported by the research councils of Finland, France, Germany, Japan, Norway, Sweden and the United Kingdom. Topical Editor M. Lester thanks two referees for their help in evaluating this paper.

References

- Barker, J. E.: Reducing bias and inefficiency in the selection algorithm, Proc. 2nd. Int. Conf. Genet. Alg., 14–21, 1987.
- Bremer, J., Hoffmann, P., Manson, A. H., Meek, C. E., Ruster, R., and Singer, W.: PMSE observations at three different frequencies in northern Europe during summer 1994, *Ann. Geophys.*, 14, 1317–1327, 1996.
- Cheong, B. L., Hoffman, M. W., and Palmer, R. D.: Efficient atmospheric simulation for high-resolution radar imaging applications, *J. Atmos. Ocean. Tech.*, 21, 374–378, 2004.
- Chilson P. B., Czechowsky, P., Klostermeyer, J., Ruster, R., and Schmidt, G.: An investigation of measured temperature profiles and VHF mesosphere summer echoes at midlatitudes, *J. Geophys. Res.*, 102, 23 819–23 828, 1997.
- Chilson, P. B., Kirkwood, S., and Häggström, I.: Frequency domain interferometry mode observations of PMSE using the EISCAT VHF radar, *Ann. Geophys.*, 18, 1599–1612, 2001.
- Chilson P. B., Yu, T.-Y., Strauch, R. G., Muschinski, A., and Palmer, R. D.: Implementation and validation of range imaging on a UHF radar wind profiler, *J. Atmos. Ocean. Tech.*, 20, 987–996, 2003.
- Cho, J. Y. N. and Röttger, J.: An updated review of polar mesosphere summer echoes: Observation, theory, and their relationship to noctilucent clouds and subvisible aerosols, *J. Geophys. Res.*, 102, 2001–2020, 1997.
- Cho, J. Y. N., Swartz, W. E., Kelley, M. C., and Miller, C. A.: CUPRI observations of PMSE during SALVO B of NLC-91: Evidence of both partial reflection and turbulent scatter, *Geophys. Res. Lett.*, 20, 2291–2294, 1993.
- Cornwell T. J.: The applications of closure phase to astronomical imaging, *Science*, 245, 263–269, 1989.
- Cornwell T. J. and Fomalont, E. B.: Synthesis imaging in radio astronomy II, *Astron. Soc. Pac.*, 180, 187–199, 1999.
- Cornwell, T. J., Braun, R., and Briggs, D. S.: Synthesis imaging in radio astronomy II, *Astron. Soc. Pac.*, 180, 151–170, 1999.
- Czechowsky, P. and Ruster, R.: VHF Radar observations of turbulent structures in the polar mesopause region, *Ann. Geophys.*, 15, 1028–1036, 1997.
- Doviak R. J. and Zrnić, D. S.: Doppler radar and weather observations, Academic Press, 1993.
- Ecklund, W. L. and Balsley, B. B.: Long-term observations of the arctic mesosphere with the MST radar at Poker Flat, Alaska, *J. Geophys. Res.*, 86, 7775–7780, 1981.
- Franke, S. J., Röttger, J., LaHoz, C., and Liu, C. H.: Frequency domain interferometry of polar mesosphere summer echoes with the EISCAT VHF radar: A case of study, *Radio Sci.*, 27, 417–428, 1992.
- Friedman P.: Radio astronomy image enhancement in the presence of phase errors using genetic algorithms, Proc. 2001 Int. Conf. Image Proces., 3, 612–615, 2001.
- Hall C.: The Ramfjordmoen MF radar (69 N, 19 E): Application development 1990–2000, *J. Atmos. Sol-Terr. Phys.*, 63, 171–179, 2001.

- Havnes, O., Melandso, F., LaHoz, C., and Aslaksen, T. K.: Charged dust in the earth's mesopause; Effects on radar backscatter, *Phys. Scripta*, 45, 535–544, 1992.
- Hill, R. J., Gibson-Wilde, D. E., Werne, J. A., and Fritts, D. C.: Turbulence-induced fluctuations in ionization and application to PMSE, *Earth Planets Space*, 51, 499–513, 1999.
- Hocking, W. K. and Röttger, J.: Studies of polar mesosphere summer echoes over EISCAT using calibrated signal strengths and statistical parameters, *Radio Sci.*, 32, 1425–1444, 1997.
- Holdsworth D. A. and Reid, I. M.: A simple model of atmospheric radar backscatter: Description and application to the full correlation analysis of spaced antenna data, *Radio Sci.*, 30, 1263–1280, 1995.
- Holland J. H.: *Adaptation in natural and artificial systems*, University of Michigan Press, 1975.
- Hoppe, U.-P., Fritts, D. C., Reid, I. M., Czechowsky, P., Hall, C. M., and Hansen, T. L.: Multiple-frequency studies of the high-latitude summer mesosphere: Implications for scattering processes, *J. Atmos. Terr. Phys.*, 52, 907–926, 1990.
- Hysell, D. L.: Radar imaging of equatorial F region irregularities with maximum entropy interferometry, *Radio Sci.*, 31, 1567–1578, 1996.
- Kudeki, E. and Sürücü, F.: Radar interferometric imaging of field-aligned plasma irregularities in the equatorial electrojet, *Geophys. Res. Lett.*, 18, 41–44, 1991.
- Lübken, F.-J., Lehmacher, G., Blix, T., Hoppe, U.-P., Thrane, E., Cho, J., and Swartz, W.: First in situ observations of neutral and plasma density fluctuations within a PMSE layer, *Geophys. Res. Lett.*, 20, 2311–2314, 1993.
- Lübken F.-J., Rapp, M., and Hoffmann, P.: Neutral air turbulence and temperatures in the vicinity of polar mesosphere summer echoes, *J. Geophys. Res.*, 107, 4273, doi:10.1029/2001JD000915, 2002.
- Luce, H., Yamamoto, M., Fukao, S., Helal, D., and Crochet, M.: A frequency domain radar interferometric imaging (FII) technique based on high resolution methods, *J. Atmos. Sol-Terr. Phys.*, 63, 221–234, 2001.
- Palmer, R. D., Yu, T.-Y., and Chilson, P. B.: Range imaging using frequency diversity, *Radio Sci.*, 34, 1485–1496, 1999.
- Rapp, M.: *Aerosol layers in the polar summer mesosphere: Interaction with the plasma of the D-region and dependence on temperature and dynamics*, Ph. D. Thesis, Bonn University, Germany, 2000.
- Rapp M. and Lübken, F.-J.: On the nature of PMSE: Electron diffusion in the vicinity of charged particles revisited, *J. Geophys. Res.*, 108, 8437, doi:10.1029/2002JD002857, 2003.
- Rapp, M., Lübken, F.-J., Müllemann, A., Thomas, G. E., and Jensen, E. J.: Small-scale temperature variations in the vicinity of NLC: Experimental and model results, *J. Geophys. Res.*, 107, 4392, doi:10.1029/2001JD001241, 2002.
- Rapp, M., Lübken, F.-J., Hoffmann, P., Latteck, R., Baumgarten, G., and Blix, T. A.: PMSE dependence on aerosol charge number density and aerosol size, *J. Geophys. Res.*, 108, 8441, doi:10.1029/2002JD002650, 2003.
- Stoica P. and Moses, R. L.: *Introduction to spectral analysis*, Prentice Hall, 1997.